Physics

Physics Research Publications

Purdue University *Year* 2004

Moments of the B meson inclusive semileptonic decay rate using neutrino reconstruction

S. E. Csorna, G. Bonvicini, D. Cinabro, M. Dubrovin, A. Bornheim, E. Lipeles, S. P. Pappas, A. Shapiro, A. J. Weinstein, R. A. Briere, G. P. Chen, T. Ferguson, G. Tatishvili, H. Vogel, M. E. Watkins, N. E. Adam, J. P. Alexander, K. Berkelman, V. Boisvert, D. G. Cassel, J. E. Duboscq, K. M. Ecklund, R. Ehrlich, R. S. Galik, L. Gibbons, B. Gittelman, S. W. Gray, D. L. Hartill, B. K. Heltsley, L. Hsu, C. D. Jones, J. Kandaswamy, D. L. Kreinick, V. E. Kuznetsov, A. Magerkurth, H. Mahlke-Kruger, T. O. Meyer, J. R. Patterson, T. K. Pedlar, D. Peterson, J. Pivarski, D. Riley, A. J. Sadoff, H. Schwarthoff, M. R. Shepherd, W. M. Sun, J. G. Thayer, D. Urner, T. Wilksen, M. Weinberger, S. B. Athar, P. Avery, L. Breva-Newell, V. Potlia, H. Stoeck, J. Yelton, B. I. Eisenstein, G. D. Gollin, I. Karliner, N. Lowrey, P. Naik, C. Sedlack, M. Selen, J. J. Thaler, J. Williams, K. W. Edwards, D. Besson, K. Y. Gao, D. T. Gong, Y. Kubota, S. Z. Li, R. Poling, A. W. Scott, A. Smith, C. J. Stepaniak, J. Urheim, Z. Metreveli, K. K. Seth, A. Tomaradze, P. Zweber, J. Ernst, K. Arms, E. Eckhart, K. K. Gan, C. Gwon, H. Severini, P. Skubic, D. M. Asner, S. A. Dytman, S. Mehrabyan, J. A. Mueller, S. Nam, V. Savinov, G. S. Huang, D. H. Miller, V. Pavlunin, B. Sanghi, E. I. Shibata, I. P. J. Shipsey, G. S. Adams, M. Chasse, J. P. Cummings, I. Danko, J. Napolitano, D. Cronin-Hennessy, C. S. Park, W. Park, J. B. Thayer, E. H. Thorndike, T. E. Coan, Y. S. Gao, F. Liu, R. Stroynowski, M. Artuso, C. Boulahouache, S. Blusk, J. Butt, E. Dambasuren, O. Dorjkhaidav, J. Haynes, N. Menaa, R. Mountain, H. Muramatsu, R. Nandakumar, R. Redjimi, R. Sia, T. Skwarnicki, S. Stone, J. C. Wang, K. Zhang, and A. H. Mahmood

Moments of the *B* meson inclusive semileptonic decay rate using neutrino reconstruction

S. E. Csorna
Vanderbilt University, Nashville, Tennessee 37235, USA

G. Bonvicini, D. Cinabro, and M. Dubrovin
Wayne State University, Detroit, Michigan 48202, USA

A. Bornheim, E. Lipeles, S. P. Pappas, A. Shapiro, and A. J. Weinstein
California Institute of Technology, Pasadena, California 91125, USA

R. A. Briere, G. P. Chen, T. Ferguson, G. Tatishvili, H. Vogel, and M. E. Watkins
Carnegie Mellon University, Pittsburgh, Pennsylvania 15213, USA

N. E. Adam, J. P. Alexander, K. Berkelman, V. Boisvert, D. G. Cassel, J. E. Duboscq, K. M. Ecklund, R. Ehrlich, R. S. Galik, L. Gibbons, B. Gittelman, S. W. Gray, D. L. Hartill, B. K. Heltsley, L. Hsu, C. D. Jones, J. Kandaswamy, D. L. Kreinick, V. E. Kuznetsov, A. Magerkurth, H. Mahlke-Krüger, T. O. Meyer, J. R. Patterson, T. K. Pedlar, D. Peterson, J. Pivarski, D. Riley, A. J. Sadoff, H. Schwarthoff, M. R. Shepherd, W. M. Sun, J. G. Thayer, D. Urner, T. Wilksen, and M. Weinberger
Cornell University, Ithaca, New York 14853, USA

S. B. Athar, P. Avery, L. Breva-Newell, V. Potlia, H. Stoeck, and J. Yelton
University of Florida, Gainesville, Florida 32611, USA

B. I. Eisenstein, G. D. Gollin, I. Karliner, N. Lowrey, P. Naik, C. Sedlack, M. Selen, J. J. Thaler, and J. Williams
University of Illinois, Urbana-Champaign, Illinois 61801, USA

K. W. Edwards
Carleton University, Ottawa, Ontario, Canada K1S 5B6 and the Institute of Particle Physics, Canada

D. Besson
University of Kansas, Lawrence, Kansas 66045, USA

K. Y. Gao, D. T. Gong, Y. Kubota, S. Z. Li, R. Poling, A. W. Scott, A. Smith, C. J. Stepaniak, and J. Urheim
University of Minnesota, Minneapolis, Minnesota 55455, USA

Z. Metreveli, K. K. Seth, A. Tomaradze, and P. Zweber
Northwestern University, Evanston, Illinois 60208, USA

J. Ernst
State University of New York at Albany, Albany, New York 12222, USA

K. Arms, E. Eckhart, K. K. Gan, and C. Gwon
Ohio State University, Columbus, Ohio 43210, USA

H. Severini and P. Skubic
University of Oklahoma, Norman, Oklahoma 73019, USA

D. M. Asner, S. A. Dytman, S. Mehrabyan, J. A. Mueller, S. Nam, and V. Savinov
University of Pittsburgh, Pittsburgh, Pennsylvania 15260, USA

G. S. Huang, D. H. Miller, V. Pavlunin, B. Sanghi, E. I. Shibata, and I. P. J. Shipsey
Purdue University, West Lafayette, Indiana 47907, USA

G. S. Adams, M. Chasse, J. P. Cummings, I. Danko, and J. Napolitano
Rensselaer Polytechnic Institute, Troy, New York 12180, USA

D. Cronin-Hennessy, C. S. Park, W. Park, J. B. Thayer, and E. H. Thorndike
University of Rochester, Rochester, New York 14627, USA

1550-7998/2004/70(3)/032002(13)/$22.50

T. E. Coan, Y. S. Gao, F. Liu, and R. Stroynowski
Southern Methodist University, Dallas, Texas 75275, USA

M. Artuso, C. Boulahouache, S. Blusk, J. Butt, E. Dambasuren, O. Dorjkhaidav, J. Haynes, N. Menaa, R. Mountain, H. Muramatsu, R. Nandakumar, R. Redjimi, R. Sia, T. Skwarnicki, S. Stone, J. C. Wang, and Kevin Zhang
Syracuse University, Syracuse, New York 13244, USA

A. H. Mahmood
University of Texas–Pan American, Edinburg, Texas 78539, USA

(CLEO Collaboration)
(Received 1 April 2004; published 17 August 2004)

We present a measurement of the composition of B meson inclusive semileptonic decays using 9.4 fb^{-1} of e^+e^- data taken with the CLEO detector at the $\Upsilon(4S)$ resonance. In addition to measuring the charged lepton kinematics, the neutrino four-vector is inferred using the hermiticity of the detector. We perform a maximum likelihood fit over the full three-dimensional differential decay distribution for the fractional contributions from the $B\to X_c\ell\nu$ processes with $X_c=D$, D^*, D^{**}, and nonresonant X_c, and the process $B\to X_u\ell\nu$. From the fit results we extract the first and second moments of the M_X^2 and q^2 distributions with minimum lepton-energy requirements of 1.0 GeV and 1.5 GeV. We find $\langle M_X^2-\overline{M}_D^2\rangle=(0.456\pm0.014\pm0.045\pm0.109)$ GeV$^2/c^4$ with a minimum lepton energy of 1.0 GeV and $\langle M_X^2-\overline{M}_D^2\rangle=(0.293\pm0.012\pm0.033\pm0.048)$ GeV$^2/c^4$ with minimum lepton energy of 1.5 GeV. The uncertainties are from statistics, detector systematic effects, and model dependence, respectively. As a test of the HQET and OPE calculations, the results for the M_X^2 moment as a function of the minimum lepton energy requirement are compared to the predictions.

DOI: 10.1103/PhysRevD.70.032002 PACS number(s): 13.20.He, 12.15.Hh, 12.39.Hg

I. INTRODUCTION

Inclusive semileptonic B meson decay can be used to measure the CKM parameters involved in the decay and to measure nonperturbative hadronic properties of the B meson. Heavy quark effective theory (HQET) combined with the operator product expansion (OPE) provides a framework in which many inclusive B decay properties can be calculated [1]. In particular, moments of the differential decay rates of a variety of processes are related to nonperturbative parameters that also appear in the calculation of the total decay rates. Measurements of these moments can therefore be used to refine calculations of the $B\to X_u\ell\nu$ and $B\to X_c\ell\nu$ decay rates and the extraction of the CKM parameters $|V_{ub}|$ and $|V_{cb}|$ from measurements of the respective branching fractions. In this paper, we present measurements of the first and second moments of the M_X^2 and q^2 kinematic variables in the decay $B\to X_c\ell\nu$, where M_X^2 and q^2 are the squares of the invariant masses of the hadronic and leptonic parts of the final state, respectively.

In the HQET and OPE framework, the inclusive B decay matrix elements are expanded in powers of $\Lambda_{\rm QCD}/M_B$. For each order in the expansion new nonperturbative parameters arise: at order $\Lambda_{\rm QCD}/M_B$, there is $\overline{\Lambda}$; at order $\Lambda_{\rm QCD}^2/M_B^2$, there are λ_1 and λ_2; and at order $\Lambda_{\rm QCD}^3/M_B^3$, there are ρ_1, ρ_2, $\mathcal{T}_1$, $\mathcal{T}_2$, $\mathcal{T}_3$, and $\mathcal{T}_4$. The nonperturbative parameter $\overline{\Lambda}$ relates the b quark mass to the B meson mass in the limit of infinite b quark mass. The λ_1 and λ_2 parameters are related to the kinetic energy of the b quark inside the B meson and the chromomagnetic moment of the b quark inside the B meson. The parameter λ_2 is directly related to the mass splitting between the B^* and B mesons. These parameters describe properties of the B meson and are not specific to the decay mode being studied. For example, the same parameters appear in expansions of the moments of the lepton energy and X_c mass distributions in $B\to X_c\ell\nu$ decays and in expansions of the moments of the photon-energy spectrum in $B\to X_s\gamma$ decays.

These calculations do not predict the long-distance effects that govern the formation of hadrons. They are therefore only applicable when a sufficiently large region of phase space is included in an observable that the hadronization effects are negligible. The differential decay rates themselves do not satisfy this condition. Instead, moments of the differential decay rates are measured and compared to the HQET-OPE predictions. The assumption made in applying quark-level calculations to hadron-level processes is known as quark-hadron duality.

We report an analysis of $B\to X\ell\nu$ decays in which both the charged lepton and the neutrino are reconstructed. We use a maximum likelihood fit to the full three-dimensional kinematic distribution to extract the exclusive branching fractions for $B\to D\ell\nu$, $B\to D^*\ell\nu$, $B\to D^{**}\ell\nu$, nonresonant $B\to X_c\ell\nu$, and $B\to X_u\ell\nu$. The descriptions of the kinematic distributions of these components used in the fit are derived from theoretical calculations or models. The extracted branching fractions are very sensitive to these models. However, the description of the inclusive differential decay rate constructed from these models and the extracted branching fractions is less model dependent, because the branching fractions have been adjusted by the fit to replicate the measured inclusive distribution. The $\langle M_X^2-\overline{M}_D^2\rangle$, $\langle(M_X^2$

$-\langle M_X^2\rangle)^2\rangle$, $\langle q^2\rangle$, and $\sqrt{\langle(q^2-\langle q^2\rangle)^2\rangle}$ moments of the $B\to X_c\ell\nu$ differential decay rate where $\overline{M}_D$ is spin averaged D meson mass, $\overline{M}_D=(M_D+3\times M_{D*})/4$, are calculated from this description and are similarly less model dependent than the branching fractions.

The moments measured in this paper can be used to determine the HQET-OPE parameters. At present, the knowledge of the $\overline{\Lambda}$ and λ_1 parameters is sufficient so that the uncertainty in the extraction of $|V_{cb}|$ from the semileptonic B meson decay rate is due to the uncertainty in the contributions from the third-order terms and second-order α_s corrections. The main goal of further moments measurements is to over-constrain the determination of $\overline{\Lambda}$ and λ_1, and thereby test the quark-hadron duality assumption. These moments could also be used to constrain the third-order terms to further improve the precision of the extraction of $|V_{cb}|$. The dependence of the moments on the minimum lepton energy used in the measurement provides an additional test of the theoretical assumptions and consistency.

II. DETECTOR AND DATA SET

The data used in this analysis were taken with two configurations of the CLEO detector, CLEO II and CLEO II.V. An integrated luminosity of 9.4 fb^{-1} was accumulated on the $\Upsilon(4S)$ resonance ($E_{\rm cm}\approx 10.58$ GeV), and an additional 4.5 fb^{-1} was accumulated at 60 MeV below the $\Upsilon(4S)$ resonance, where there is no $B\overline{B}$ production. Both detector configurations covered 95% of the 4π solid angle with drift chambers and a cesium iodide calorimeter. Particle identification was provided by muon chambers with measurements made at material depths of 3, 5, and 7 hadronic interaction lengths, a time-of-flight system and specific ionization (dE/dx) measured in the drift chamber. In the CLEO II configuration, there were three concentric drift chambers filled with a mixture of argon and ethane. In the CLEO II.V detector, the innermost tracking chamber was replaced with a three-layer silicon detector and the main drift chamber gas was changed to a mixture of helium and propane. The CLEO II and II.V detectors are described in more detail in Refs. [2] and [3].

III. EVENT SELECTION AND RECONSTRUCTION

Events are selected to have an identified electron or muon with momentum greater than 1 GeV/c and a well-reconstructed neutrino. Additional criteria are used to suppress background events from the $e^+e^-\to q\overline{q}$ continuum under the $\Upsilon(4S)$ resonance, where q is u, d, s, or c.

The identified leptons are required to fall within the barrel region of the detector ($|\cos\theta|<0.71$, where θ is the angle between the lepton momentum and the beam axis). Electrons are identified with a likelihood-based discriminator which combines dE/dx, time-of-flight, and the ratio of the energy deposited in the calorimeter to the momentum of the associated charged track (E/p). Muons are identified by their penetration into the muon chambers. For momenta between 1.0 and 1.5 GeV/c, muon candidates are required to penetrate at least 3 interaction lengths and above 1.5 GeV/c, candidates are required to penetrate at least 5 interaction lengths. The lepton-identification efficiencies are calculated by embedding raw data from reconstructed leptons in radiative QED events into hadronic events. The rate at which pions and kaons fake leptons is measured by reconstructing $K_S^0\to\pi^+\pi^-$, $D^0\to K^-\pi^+$, and $\overline{D^0}\to K^+\pi^-$ using only kinematics and then checking the daughter particle lepton-identification information.

Neutrinos are reconstructed by subtracting the sum of the four-momenta of all observed tracks and showers not associated with tracks, $p^\mu_{\rm observed}$, from the four-momentum of the e^+e^- initial state, $p^\mu_{e^+e^-}$, which is nearly at rest in the laboratory:

$$p^\mu_\nu=p^\mu_{e^+e^-}-p^\mu_{\rm observed}.$$

The errors made in this assumption are due to particles lost through inefficiency or limited acceptance, fake tracks and showers, and other undetected particles such as K_L^0 mesons, neutrons, or additional neutrinos. Several requirements are made to select events in which these effects are reduced and the neutrino four-momentum resolution is correspondingly improved.

Because extra neutrinos are correlated with extra charged leptons, events with an identified lepton in addition to the signal lepton are rejected. The primary source of fake tracks is charged particles that do not have sufficient transverse momentum to reach the calorimeter and therefore curl in the tracking chambers, returning to the beam axis. The drift chamber hits produced by such a particle after its initial outbound trajectory may be reconstructed as additional tracks. Criteria have been developed to identify such errors and make a best estimate of the actual charged particles in the event. Events for which the net charge of the all tracks selected by these criteria is not zero are removed, reducing the effect of lost or fake tracks. Showers in the calorimeter that are matched to tracks in the drift chamber are not used, to avoid double-counting their energy. A neural network algorithm provides further rejection of secondary hadronic showers associated with showers that are matched with tracks.

A final neutrino reconstruction quality requirement is that the mass of the reconstructed neutrino must be small. The ratio of the reconstructed neutrino invariant mass squared to twice the reconstructed neutrino energy is required to satisfy $|M^2_\nu/2E_\nu|<0.35$ GeV/c^4. This quantity is approximately proportional to the energy of a lost or fake particle. After this cut, the reconstructed neutrino's energy is assigned to be the magnitude of the missing momentum, because the momentum is not dependent on the particle identification of the tracks and so has a better resolution than the direct energy measurement. The resulting neutrino energy resolution has a narrow core with a full width at half maximum height of approximately 120 MeV and a broad tail of over estimation of the neutrino energy which extends up to 1.5 GeV.

Continuum events are suppressed by a combination of event-shape and -orientation criteria. These exploit the tendency of continuum events to be jet-like and aligned with the

beam axis, in contrast with $B\overline{B}$ events which are more spherical and randomly oriented in the detector. The ratio of second to the zeroth Fox-Wolfram moment [4], $R_2 = H_2/H_0$, of the energy flow in the event is required to be less than 0.4. In addition, a neural network is used to combine R_2, the angle between the lepton and the event thrust axis, the angle between the lepton momentum and the beam axis, and the fraction of the total energy lying in nine separate cones around the lepton direction, which cover the full 4π solid angle. The R_2 cut is more than 99% and 95% efficient for $B\to X_c\ell\nu$ and $B\to X_u\ell\nu$, respectively, while removing 60% of the continuum events. The neural-net cut removes an additional 73% of the continuum background, while keeping 92% and 94% of $B\to X_c\ell\nu$ and $B\to X_u\ell\nu$, respectively.

After all cuts we observe 121851 events from the data sample collected on the $\Upsilon(4S)$ resonance. The overall efficiency varies from 1.5% for $B\to X_c\ell\nu$ nonresonant to 4.2% for $B\to X_u\ell\nu$.

IV. KINEMATIC VARIABLES

The differential decay rate of inclusive semileptonic B meson decays can be described in terms of three independent kinematic variables, which can be chosen to be the squares of the masses of the hadronic and leptonic parts of the final state (M_X^2 and q^2) and the cosine of the helicity angle of the virtual W ($\cos\theta_{W\ell}$). The helicity angle is defined as the angle between the lepton momentum in the virtual-W frame and the virtual-W momentum in the B meson frame.

Because we do not reconstruct the hadronic part of the final state, M_X^2 must be inferred through kinematics:

$$M_X^2 = M_B^2 + q^2 - 2E_{\rm beam}(E_\ell + E_\nu) + 2|\vec{p}_B||\vec{p}_\ell + \vec{p}_\nu|\cos\theta_{B\cdot\ell\nu}, \tag{1}$$

where $\vec{q} = \vec{p}_\ell + \vec{p}_\nu$ is the momentum of the lepton system, $\vec{p}_B$ is the momentum of the B, and $\theta_{B\cdot\ell\nu}$ is the angle between them. Since the B mesons are the daughters of an $\Upsilon(4S)$ produced at rest, the magnitude of the B momentum is known and small ($|\vec{p}_B| \approx 300$ MeV), however its direction is unmeasured. The last term in the M_X^2 formula depends on the B momentum direction, and is small, unmeasured, and neglected in this analysis. Because of the neglected term, the M_X^2 resolution depends on $|\vec{q}|$. In addition, because of the unknown B momentum direction, the B meson frame in the definition of $\cos\theta_{W\ell}$ is replaced by the lab frame in the definition of the reconstructed quantity.

V. COMPOSITION EXTRACTION

The full three-dimensional differential decay rate distribution as a function of the reconstructed quantities q^2, M_X^2, and $\cos\theta_{W\ell}$ is fitted for the contributions from semileptonic B decay and backgrounds. The q^2 variable is replaced by $q^2/(E_\ell + E_\nu)^2$ for fitting purposes. This has the effect of varying the q^2 bin size as a function of $E_\ell + E_\nu$. The B decay modes are $B\to D\ell\nu$, $B\to D^*\ell\nu$, $B\to D^{**}\ell\nu$, $B\to X_c\ell\nu$ nonresonant, and $B\to X_u\ell\nu$. The backgrounds are classified as secondary leptons, continuum leptons, or fake leptons. A secondary lepton is a real lepton in a $B\overline{B}$ event whose parent is not a B meson. A continuum lepton is a real lepton in a continuum $e^+e^-\to q\overline{q}$ event. A fake lepton is a non-leptonic track from either a $B\overline{B}$ or a continuum event which is identified as a lepton.

We perform a binned maximum-likelihood fit where component histograms are constructed from weighted Monte Carlo or data events. The fit uses electrons and muons simultaneously, with a separate set of histograms for each. The likelihood is implemented to take into account the histogram statistics using the method described in Ref. [6].

The $B\to X\ell\nu$ modes, secondary leptons and real leptons from the continuum are modeled with events from a GEANT [7] simulation of the CLEO detector that are reconstructed in the same manner as data events. The $B\to D\ell\nu$ and $B\to D^*\ell\nu$ modes are simulated with an HQET-based model using the PDG [8] averages of measurements of the form factors rescaled to have the curvature term set to 50% of its theoretically predicted value (see Sec. VI D). The $B\to D^{**}\ell\nu$ and $B\to X_u\ell\nu$ modes are simulated using form factors from the ISGW2 model [9]. The X_c nonresonant modes are simulated with the Goity and Roberts model [10] in which the D and D^* contributions are excluded.

The fake leptons are modeled with data events where a track is selected to be treated as a lepton. The events are unfolded bin by bin in the lepton energy to extract the π and K contributions, which are then multiplied by the measured fake rates. This models fake leptons from both $B\overline{B}$ and continuum. This method also provides an absolute normalization for the fake-lepton contribution to the data sample. The real leptons from the continuum are modeled with a Monte Carlo simulation which has been tuned to replicate the appropriate charm spectra; charm is the source of most leptons from continuum. The models of both continuum and fake leptons have been validated and constrained by comparisons with the 4.5 fb^{-1} of off-resonance data. The secondary leptons are modeled with CLEO's generic $B\overline{B}$ Monte Carlo which has also been tuned to replicate measured charm spectra and semileptonic charm-decay measurements. The measured branching fractions for B meson decays to charmed final states do not sum to the theoretical prediction for the inclusive rate [11]. This discrepancy referred to as the charm counting problem is most likely due to missing or mismeasured modes in the sum. The branching fractions in the $B\overline{B}$ Monte Carlo simulation are therefore tuned to saturate the theoretically predicted level of charm production.

Final-state radiation (FSR) can play an important role in semileptonic decays. This is particularly important for events with an electron in the final state, because the small electron mass enhances the effect. For the $B\to X_c\ell\nu$ modes, the Monte Carlo events simulated with GEANT include the effects of radiation using the PHOTOS package [13] to generate radiated photons. This simulated both the physics of radiation and the detector response to the photons. For the $B\to X_u\ell\nu$ modes and the $e^+e^-\to q\overline{q}$ continuum Monte Carlo

TABLE I. Composition of the data sample and summary of the models used in the fit.

Mode	Fraction of Data Sample	Model
$B\to D\ell\nu$	0.118	HQET [5]
$B\to D^*\ell\nu$	0.476	HQET [5]
$B\to D^{**}\ell\nu$	0.084	ISGW2 [9]
Nonresonant $B\to X_c\ell\nu$	0.033	Goity and Roberts [10]
$B\to X_u\ell\nu$	0.016	ISGW2 [9]
Secondary Leptons	0.050	CLEO B decay model and measurements of semileptonic charm hadron decay
Fake Leptons	0.132	Data and measured lepton fake rates
Electron	0.002	
$E_\mu<1.5$ GeV	0.100	
$E_\mu\geqslant 1.5$ GeV	0.030	
Continuum Leptons	0.089	JETSET [12] with normalization from data

events, the events were simulated without FSR and an algorithm to apply the FSR after the detector simulation is used. This algorithm generates photons and calculates the effect on the lepton four-vectors in the same way as the PHOTOS package. The change in the lepton momenta is then applied to the reconstructed leptons. The effect of losing a photon is simulated using a random number to apply the photon efficiency extracted from the GEANT simulation. If the photon is rejected, its four-vector is added to the neutrino four-vector simulating the effect of the additional lost particle on the reconstructed neutrino kinematics.

The normalization of the continuum lepton component is determined from the data taken below $B\overline{B}$ threshold. The normalization of the fake leptons is determined from the measured fake rates and the measured track spectra. The contributions of these two backgrounds are therefore not allowed to vary in the fit, while those of the secondary leptons and all of the $B\to X\ell\nu$ modes are. A summary of the processes contributing to the selected sample, the fraction of the sample each contributes, and the models used to describe them in the fit is shown in Table I. The contribution fractions are either determined by the fit or externally constrained as described above.

Projections of the Monte Carlo simulations of reconstructed quantities q^2, M_X^2, and $\cos\theta_{W\ell}$ for the various $B\to X\ell\nu$ modes are shown in Fig. 1. These one-dimensional projections illustrate some of the discriminating power available to the full three-dimensional fit. Projections of the data and fit result, shown in Fig. 2, are compatible with each other within the estimated size of the systematic uncertainties.

From the fit results the branching fractions are determined using the efficiency as predicted by the Monte Carlo simulation, the data yield, and the number of $B\overline{B}$ pairs in the data sample. The resulting branching fractions are shown in Table II.

VI. SYSTEMATIC UNCERTAINTIES

The method of neutrino reconstruction adds a large amount of kinematic information to each event. However, it also adds significant potential for systematic errors. The Monte Carlo simulation of resolution on the neutrino kinematics is affected by the modeling of the signal, the other B in the event, and the detector response. The GEANT Monte Carlo simulation does not perfectly reproduce the track and shower efficiencies and fake rates, nor are B decays well enough understood that the inclusive particle distributions are well known. For this analysis we employ a reweighting method in order to quantify the effects of these uncertainties on our results. For example, to study the effect of the tracking efficiency uncertainty, the Monte Carlo events in which tracks are lost are given a higher or lower weight in constructing the component histograms used in the fit.

The shifts of the nominal result due to variations of the detector performance, the modeling of inclusive B and D meson decay, and radiative corrections are summed in quadrature to get the total detector systematic uncertainty. The shifts for each variation of the signal B model are similarly summed in quadrature to get the total model-dependence systematic. The larger contributions to the systematic uncertainties are summarized in Table III.

A. The modeling of inclusive B and D decay

The probability that the full set of final-state particles in an event will be found depends on the number of particles, their momenta and their type. The model of the B and D decay physics used in the Monte Carlo is tuned to reproduce a wide variety of inclusive and exclusive measurements. We have identified a number of inclusive properties to which the neutrino resolution and the efficiency of the event selection are particularly sensitive. These are the number of K_L^0 mesons, baryons, and extra neutrinos in the final state, and the total charged particle and photon multiplicities.

The extra neutrinos in the events come predominantly from semileptonic decays of the other B meson in the event, and from secondary charm-decays, $B\to c\to x\ell\nu$. These are both suppressed by the second-lepton veto, but because of the energy threshold for the lepton identification, there is a significant unvetoed contribution. The branching fraction $\mathcal{B}(B\to c\to x\ell\nu)$ calculated from the measured charm production and charm semileptonic branching fractions is $9.6\pm 0.9\%$ [8]. However, the branching fractions for charm pro-

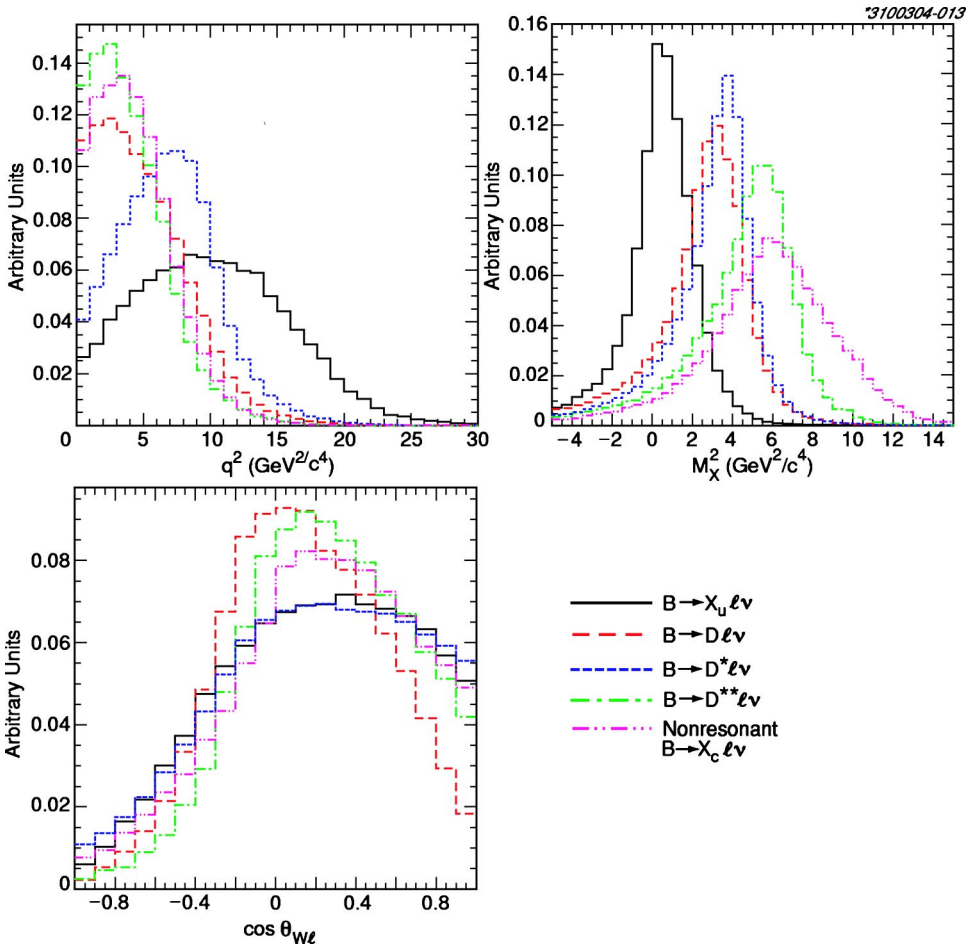

FIG. 1. Monte Carlo simulation of the distributions of the reconstructed quantities q^2, M_X^2, and $\cos\theta_{W\ell}$ for the various $B \to X\ell\nu$ modes. The curves are normalized to have unit area to facilitate comparison of the shapes. Note that due to imperfect resolution M_X^2 can be less than zero.

duction in B meson decay are not consistent with the theoretically predicted rate [11]. The inclusive B decay model used in the simulation, which is consistent with the theoretical prediction, gives a higher rate of 10.7%. Based on these numbers the systematic uncertainty assigned to this rate is $\pm 1.1\%$.

The number of baryons in B meson decay is determined from measurements of the branching fraction $\mathcal{B}(B \to (p \text{ or } \bar{p})X) = 8.0 \pm 0.4\%$ [8]. Because of the uncertainty in the exclusive composition of the process, the number of $B \to$baryons events in the simulation is varied by $\pm 20\%$.

The number of K_L^0 mesons is inferred from a measurement of the inclusive number of K_S^0 mesons in B decay. The discrepancy between this measurement and the value used in the simulation is 7%. The number of K_L^0 mesons is therefore conservatively varied by $\pm 10\%$.

To assess the uncertainty due to the charged particle and photon multiplicities of inclusive B decay, simulated events are reweighted to correctly reproduce track and shower multiplicities observed in the data sample. The full shift is used as an estimate of the uncertainty.

B. The detector response

The effect of the detector response enters through the lepton-identification efficiency and fake rate, and the neutrino energy resolution and efficiency. The lepton-identification efficiency is varied between the efficiencies determined by the embedding procedure described above, and the Monte Carlo simulation. The shift is larger than the statistical errors on the embedding measurement. This conservatively estimates the effect of a systematic shift, and shows lepton efficiency to be a very small contribution to the uncertainty.

The uncertainty due to lepton fake rates is determined by using Gaussian distributed random numbers to vary the fake rates within their experimental errors. These variations are then propagated through the fake lepton model for a maximum of ten trials. The shift of the results due to an increase or decrease of the total rate is also included.

The neutrino-momentum resolution and event-selection efficiency are strongly affected by how well the tracks and showers observed correspond to the actual number of charged particles and photons produced in the event. This correspondence is affected by the track and shower efficiency and fake rate.

The uncertainty on the charged particle efficiency is determined using the constraints of charge conservation in 1-prong versus 3-prong τ pair events to infer when a track has been lost. Monte Carlo simulated tracks embedded in hadronic data events are used to study the effect of the event environment on the tracking efficiency. The uncertainty on the photon efficiency is determined by varying the inputs

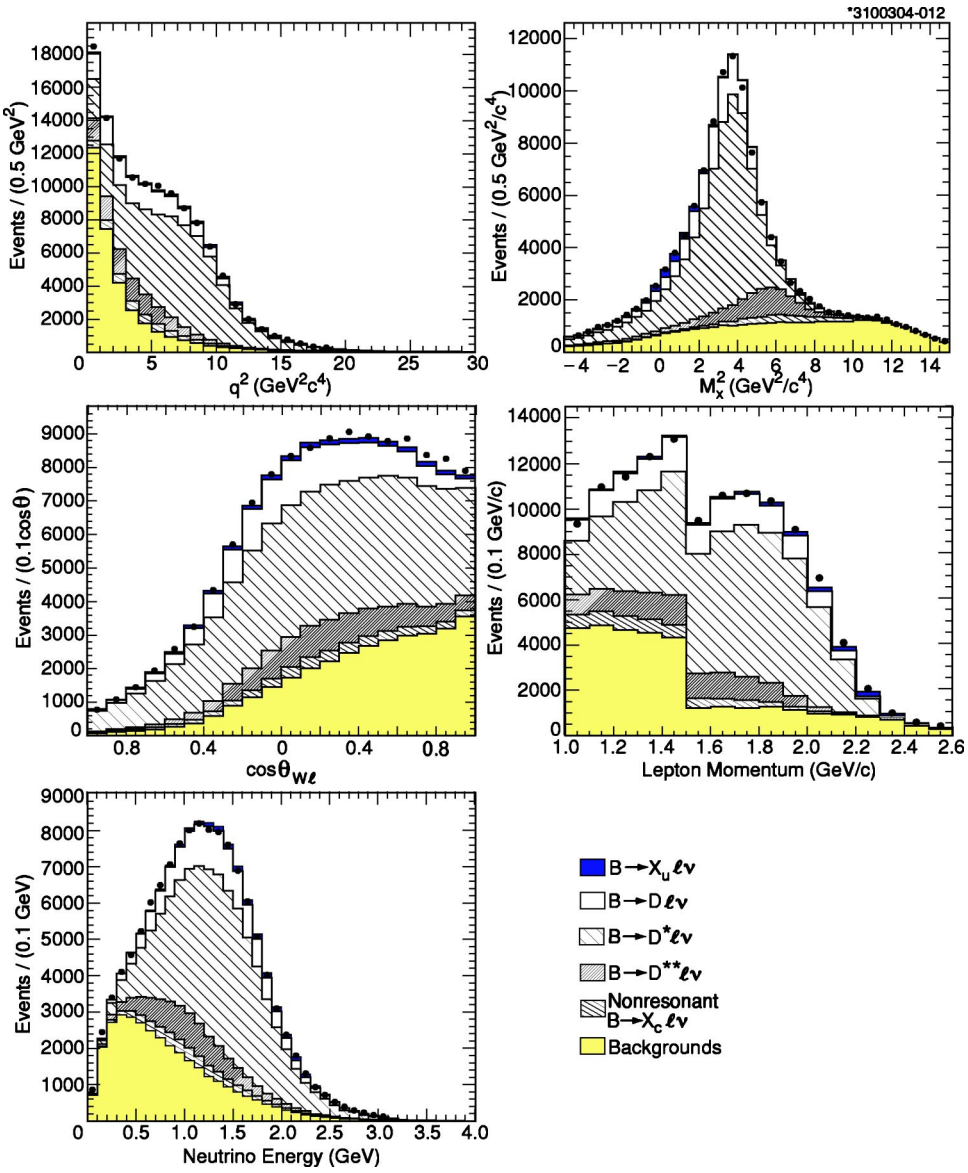

FIG. 2. Projections of the fit results in the reconstructed quantities. The histograms are the Monte Carlo simulation and the points with error bars are the data. The step in the lepton-momentum distribution is due to the looser muon identification used below 1.5 GeV/c for which there is a higher fake rate and higher efficiency.

into the Monte Carlo simulation and by comparing the shower shape distributions observed in data with the Monte Carlo simulation. Both of these Monte Carlo studies are described in detail in reference [14].

Tracks identified by the reconstruction software that do not correspond to actual charged particles produced in the collisions are referred to as fake tracks. The uncertainty of the Monte Carlo prediction for the number of fake tracks is estimated using 1-prong versus 3-prong τ pair events with an extra track and the total charge distribution of the event sample.

The largest detector-related uncertainty is the number of reconstructed showers that are not due to photons. The main cause of these showers is secondary hadronic interactions of the particles produced in the primary showers of charged hadrons. The reliability of the Monte Carlo simulation of these showers has been studied in $\gamma\gamma\to K_S^0 K_S^0$ events and in $\tau^\pm\to\pi^\pm\pi^0\nu_\tau$ events. In both cases, the expected number of photons in the detector is well defined for the specified mode. The number of observed showers is then compared to the number of showers predicted by a Monte Carlo simulation. These measurements are imprecise because of the uncertainty in the contributions of other modes to the selected sample. Based on these comparisons, a variation of the number of fake photons by $\pm 10\%$ is used to assign an uncertainty.

TABLE II. Branching fractions results. The errors on the entries in the table are the statistical, detector systematic, and model dependence uncertainties, respectively.

Mode	Branching Fraction ($\times 10^{-2}$)
$B\to D\ell\nu$	$1.92\pm0.08\pm0.19\pm0.74$
$B\to D^*\ell\nu$	$6.37\pm0.06\pm0.65\pm0.86$
$B\to D^{**}\ell\nu$	$1.51\pm0.07\pm0.30\pm0.52$
Nonresonant $B\to X_c\ell\nu$	$0.70\pm0.07\pm0.25\pm0.62$
$B\to X_u\ell\nu$	$0.12\pm0.01\pm0.03\pm0.23$
Sum	$10.61\pm0.29\pm1.09\pm0.75$

TABLE III. Contributions to the systematic uncertainties of the branching fraction measurements. The entries are given as a percentage of the central value. The entries separated by a slash indicate the effect of raising and lowering the varied quantity, respectively. The uncertainties quoted for the $B\to X_c\ell\nu$ nonresonant mass distribution and $B\to X_u\ell\nu$ models represent the range covered by the set of models studied.

Variation	$B\to D\ell\nu$	$B\to D^*\ell\nu$	$B\to D^{**}\ell\nu$	Nonresonant $B\to X_c\ell\nu$	$B\to X_u\ell\nu$	Inclusive $B\to X\ell\nu$
Statistical	3.9	0.9	4.9	10.1	7.0	2.7
Detector	10.1	10.2	20.0	35.2	25.5	10.3
Model Dep.	38.7	13.5	34.2	88.7	201.5	7.0
Lepton Fake Rate	0.8/−0.6	0.4/−0.3	2.7/−1.8	6.9/−2.8	12.6/−6.3	0.8/−0.2
Continuum ±10%	−3.6/2.6	0.4/−0.5	−2.9/6.7	1.7/−6.3	−4.1/4.6	−0.8/0.7
$\mathcal{B}(b\to c\to\ell)$ ±10%	1.9/−2.0	2.6/−2.5	6.6/−6.3	−0.8/0.7	−6.1/6.4	2.7/−2.6
$\mathcal{B}(b\to$baryons) ±20%	1.7/−0.9	3.9/−3.0	4.9/−3.9	1.7/−1.0	−0.1/0.9	3.4/−2.6
No. K_L^0	2.4/−2.4	2.6/−2.5	7.0/−6.7	−1.3/1.2	−7.2/7.7	2.8/−2.7
Track Efficiency	−4.8/4.9	−5.8/6.0	−9.6/10.8	0.9/−1.7	−1.7/1.7	−5.6/5.9
No. Fake Tracks	1.9/−1.7	2.3/−2.0	2.6/−2.3	−3.9/3.5	0.3/−0.2	1.9/−1.6
Shower Efficiency	−2.2/2.5	−1.4/1.7	−3.9/4.8	1.8/−1.4	−3.8/3.7	−1.7/2.1
No. Fake Showers	−3.1/2.7	−0.5/0.2	4.5/−3.9	−28.2/27.5	−14.7/15.3	−2.2/2.0
Track Multiplicity	2.5	2.0	3.1	2.2	−3.0	2.2
Shower Multiplicity	2.2	3.4	3.8	8.9	−3.4	3.5
Final-State Radiation	−0.1	−3.3	−0.2	9.0	−7.2	−1.5
Lepton Efficiency	4.3	2.0	4.1	5.1	−3.7	2.8
$B\to D\ell\nu$ ρ Param.	6.4/−5.2	−2.6/1.8	4.6/−2.0	−5.4/2.3	0.1/0.2	−0.1/0.0
$B\to D\ell\nu$ c Param.	1.4/−1.1	−0.5/0.3	0.8/−0.4	−0.5/0.2	0.1/−0.0	0.1/−0.1
$B\to D^*\ell\nu$ ρ Param.	32.4/−32.1	−11.4/11.0	17.9/−15.2	−18.0/17.0	6.3/−4.8	0.4/−0.3
$B\to D^*\ell\nu$ c_{A_1} Param.	−1.1/0.8	0.8/−0.7	−1.0/0.6	2.9/−2.0	1.1/−1.0	0.3/−0.3
$B\to D^*\ell\nu$ R1/R2 1st Eig. Vec.	−13.3/14.9	3.5/−3.7	−10.0/10.1	16.7/−15.3	−4.5/5.7	−0.7/1.0
$B\to D^*\ell\nu$ R1/R2 2nd Eig. Vec.	9.9/−10.4	−4.0/4.2	3.2/−3.4	0.9/−0.7	−3.3/3.5	−0.1/0.2
$B\to D^{**}\ell\nu$ HQET Model	−4.0	0.5	2.3	0.1	0.2	−0.1
$B\to D^{**}\ell\nu$ w Slope	−2.7/3.1	0.9/−0.8	−2.7/0.6	13.6/−9.8	−0.5/0.2	0.5/−0.5
$B\to X_c\ell\nu$ Nonres w Slope	−0.0/−0.1	0.1/−0.0	−6.3/3.6	17.4/−9.9	−0.2/0.1	0.3/−0.2
$B\to X_c\ell\nu$ Nonres Mass	1.0/−6.2	1.0/−2.9	25.6/−4.9	81.8/−13.5	2.5/0.2	6.9/−2.7
$B\to X_u\ell\nu$ Model	3.0/−3.0	0.2/−1.5	0.8/−2.3	0.9/−6.7	201.2/−19.4	0.5/−0.2

C. Radiative corrections

PHOTOS implements an algorithm based on a splitting function that applies the same physics at $\mathcal{O}(\alpha)$ as the prescription of Atwood and Marciano [15]. PHOTOS also modifies the kinematics of the decay to force the conservation of momentum in addition to energy. The PHOTOS algorithm implements an approximation that ignores the internal structure of the hadronic system. Richter-Wąs [16] has made a comparison of the PHOTOS and Atwood-Marciano prescriptions with an exact order-α calculation of the radiative corrections to the $B^-\to D^0\ell^-\overline{\nu}$ differential decay rate and has found agreement at the 20% and 30% level, respectively. Because we must extrapolate to the other $B\to X_c\ell\nu$ modes, we make a conservative estimate that the PHOTOS calculation can be trusted to ±50%.

D. Signal mode model dependence

The models for all the $B\to X\ell\nu$ components were varied to assess the model dependence of the measured branching fractions. The exclusive $B\to D\ell\nu$ and $B\to D^*\ell\nu$ modes have been studied extensively in variety experiments [8]. The $B\to D\ell\nu$ differential decay rate is modeled with

$$\frac{d\Gamma}{dw}=\frac{G_F^2|V_{cb}|^2}{48\pi^3}M_B^5(1+r)^2r^3(\omega^2-1)^{3/2}\xi(w)^2,$$

where $r=M_D/M_B$ and

$$\xi(w)=\xi(1)(1-\rho_D^2(w-1)+c_D(w-1)^2)$$

is the Isgur-Wise function. After integrating out unmeasured angles the differential decay rate for the $B\to D^*\ell\nu$ mode is

$$\frac{d\Gamma}{dw\,d\cos\theta_{W\ell}}=\frac{G_F^2|V_{cb}|^2M_B^5}{(4\pi)^3}r^{*3}(1-r^*)^2(w^2-1)(w+1)^2h_{A_1}(w)^2\left[\sin\theta_{Wl}^2\left(1+\frac{w-1}{1-r^*}(1-R_2)\right)^2+\cos\theta_{W\ell}^2\left(1+\frac{w-1}{w+1}R_1^2\right)\right.$$

TABLE IV. Variations of the $B\to D\ell\nu$ and $B\to D^*\ell\nu$ form factors.

	$B\to D\ell\nu$		$B\to D^*\ell\nu$	
Variation	ρ_D^2	c_D	$\rho_{A_1}^2$	c_{A_1}
Nominal	0.80	0.56	1.20	0.7
Raise linear coefficient	1.13	0.67	1.48	0.8
Lower linear coefficient	0.48	0.44	0.91	0.58
Raise quadratic coefficient	1.22	1.12	1.51	1.39
Lower quadratic coefficient	0.39	0.0	0.88	0.0

$$+4R_1\cos\theta_{W\ell}\sqrt{\frac{w-1}{w+1}}\Bigg],$$

where $r^*=M_{D^*}/M_B$ and the form-factor $h_{A_1}(w)$ is expanded as

$$h_{A_1}(w)=h_{A_1}(w)(1)(1-\rho_{A_1}^2(w-1)+c_{A_1}(w-1)^2).$$

The form-factor parameters ρ_D^2, $\rho_{A_1}^2$, R_1, and R_2 were varied within the range of the errors on the form-factor measurements. The coefficients of the quadratic terms c_D and c_{A_1} have not been measured and are usually constrained by theoretical predictions [17]. Because the data have an excess above the model in the q^2 region between 5 and 8 GeV$^2/c^4$, these parameters were set to 50% of their predicted values and varied by $\pm 50\%$ of the predictions. The small discrepancy in the 5 to 8 GeV$^2/c^4$ region of the q^2 distribution in Fig. 2 is more pronounced when the quadratic terms are constrained to their predicted values. The resulting parameter values used for the nominal results and those used to evaluate the model dependence are summarized in Table IV.

To assess the dependence on the $B\to D^{**}\ell\nu$ model, the ISGW2 model of the $B\to D^{**}\ell\nu$ form-factors [9] used for the nominal result was replaced by a model inspired by HQET calculations [18]. The slope of the $B\to D^{**}\ell\nu$ and nonresonant $B\to X_c\ell\nu$ form factors in the q^2 dimension was also varied.

The dominant model dependence of the moments results (see Sec. VII) is due to the hadronic mass distribution of the $B\to X_c\ell\nu$ nonresonant mode. This is conservatively reweighted with a series of Gaussians restricted to the kinematically allowed region. The means of the Gaussians are allowed to range from M_D+M_π to 3.5 GeV/c^2, with variances ranging from 0.25 GeV$^2/c^4$ to 1.25 GeV$^2/c^4$.

The $B\to X_u\ell\nu$ simulation is varied from an all-nonresonant model to the nominal ISGW2 model [9], with a hybrid of the two in between. The all-nonresonant model differential decay rate corresponds to the prediction of HQET combined with CLEO's measurement of the $B\to X_s\gamma$ spectral function [19,20].

The maximum deviation of the nonresonant $B\to X_c\ell\nu$ mass Gaussian variations is added in quadrature with the deviation of the other model variations to get the total model dependence.

VII. CALCULATION OF MOMENTS

The branching fraction of the individual components, $\mathcal{B}_m$, combined with the physics models used in the fit form a description of the inclusive differential decay rate. It is from this description that the moments results are calculated. A moment $\langle M\rangle$ with a cut C is expressed as

$$\langle M\rangle_C=\frac{\Sigma_m m_m c_m \mathcal{B}_m}{\Sigma_m c_m \mathcal{B}_m}, \tag{2}$$

where c_m is the fraction of the decay rate for mode m in the region defined by the cut,

$$c_m\equiv\frac{\int\frac{d\Gamma_m}{d\vec{x}}C(\vec{x})d\vec{x}}{\int\frac{d\Gamma_m}{d\vec{x}}d\vec{x}}, \tag{3}$$

and m_m is the moment of the mode m in that region,

$$m_m\equiv\frac{\int M(\vec{x})\frac{d\Gamma_m}{d\vec{x}}C(\vec{x})d\vec{x}}{\int\frac{d\Gamma_m}{d\vec{x}}C(\vec{x})d\vec{x}}. \tag{4}$$

The quantities m_m and c_m depend only on the model. The measured branching fractions, $\mathcal{B}_m$, depend on the model, the detector simulation, and the data. Since the branching fractions are measured using the inclusive differential decay rate, when combined with the models used in the fit they give a good description of the true differential decay rate. Mismodeling of a contribution may cause the branching fraction to be mismeasured, but the shape will still be well described. For instance, the main separation of the D and D^* modes is due to the q^2 distribution. If the q^2 slope of either of these modes is mismodeled, the relative rates of the modes will be affected, but the model of the q^2 distribution and its moments will be only weakly affected.

A. Radiative corrections

Radiative corrections play an important role in the measurement of the M_X^2 distribution. The reconstructed M_X^2 is defined to be the system recoiling against the charged lepton and the neutrino. If a photon is radiated by the lepton in the event, it will be included in this definition of the recoil system,

$$M_X^2=(p_B^\mu-p_\ell^\mu-p_\nu^\mu)^2=(p_h^\mu+p_\gamma^\mu)^2. \tag{5}$$

The goal of this analysis is to measure the mass-squared moment of the recoiling hadronic system p_h^2, not its combination with the radiated photon $(p_h+p_\gamma)^2$. To correct for this effect, the data are fit using fully simulated GEANT Monte Carlo events in which the PHOTOS package [13] has been used to generate radiated photons. The moments are calculated from the fit results and the models without radia-

TABLE V. Moments results with $E_\ell > 1.0$ GeV and $E_\ell > 1.5$ GeV lepton-energy cuts. The errors on the entries in the table are the statistical, detector systematic, and model dependence uncertainties, respectively.

Moment	$E_\ell > 1.0$ GeV	$E_\ell > 1.5$ GeV
$\langle M_X^2 - \overline{M}_D^2 \rangle$ (GeV$^2/c^4$)	$0.456 \pm 0.014 \pm 0.045 \pm 0.109$	$0.293 \pm 0.012 \pm 0.033 \pm 0.048$
$\langle (M_X^2 - \langle M_X^2 \rangle)^2 \rangle$ (GeV$^4/c^8$)	$1.266 \pm 0.065 \pm 0.222 \pm 0.631$	$0.629 \pm 0.031 \pm 0.088 \pm 0.113$
$\langle q^2 \rangle$ (GeV$^2/c^4$)	$4.892 \pm 0.015 \pm 0.094 \pm 0.100$	$5.287 \pm 0.020 \pm 0.073 \pm 0.095$
$\sqrt{\langle (q^2 - \langle q^2 \rangle)^2 \rangle}$ (GeV$^2/c^4$)	$2.852 \pm 0.002 \pm 0.003 \pm 0.047$	$2.879 \pm 0.006 \pm 0.007 \pm 0.049$

tive corrections of the hadronic mass distributions for each mode and thus do not have a shift due to the radiative corrections.

The application of the radiative corrections is further complicated by the fact that the generated photons are low energy and often lost. When the photon is lost it can cause the event to fail the missing-mass cut. If the event does pass the missing-mass cut, the reconstructed neutrino will be biased toward high energy, pushing the reconstructed M_X^2 toward the true hadronic mass without the photon. If neglected, this would increase the measured $\langle M_X^2 - \overline{M}_D^2 \rangle$ moment with a 1.0 GeV lepton-energy cut by 0.082 GeV$^2/c^4$, before detector effects are included. This is reduced to 0.037 GeV$^2/c^4$ after detector effects. The variation used to assign the systematic uncertainty due to the radiative corrections is discussed in Sec. VI C.

B. Results

The resulting $\langle M_X^2 - \overline{M}_D^2 \rangle$, $\langle (M_X^2 - \langle M_X^2 \rangle)^2 \rangle$, $\langle q^2 \rangle$, and $\sqrt{\langle (q^2 - \langle q^2 \rangle)^2 \rangle}$ moments of the $B \to X_c \ell \nu$ differential decay rate with their uncertainties are presented in Table V. The corresponding correlation coefficients are shown in Table VI. These correlations included statistical, systematic, and model-dependence uncertainties. Because the moments measured with a 1.0 GeV and a 1.5 GeV lepton-energy cut are highly correlated, it is also useful to consider the difference between the $\langle M_X^2 - \overline{M}_D^2 \rangle$ moment with the two different cuts. We find

$$\langle M_X^2 \rangle_{E_\ell > 1.0\ \mathrm{GeV}} - \langle M_X^2 \rangle_{E_\ell > 1.5\ \mathrm{GeV}} = (0.163 \pm 0.014 \pm 0.036 \pm 0.064)\ \mathrm{GeV}^2/c^4$$

and a correlation coefficient of this value with the $\langle M_X^2 - \overline{M}_D^2 \rangle_{E_\ell > 1.5\ \mathrm{GeV}}$ moment of 0.486. The $\langle M_X^2 - \overline{M}_D^2 \rangle$ moments as a function of the lepton energy are shown in Table VII. The contributions of the individual systematic uncertainties for the moments results with a 1.0 GeV lepton-energy cut are shown in Table VIII.

VIII. CONCLUSION

We have measured the first and second moments of the M_X^2 and q^2 distributions in the inclusive process $B \to X_c \ell \nu$. Results are presented with minimum lepton-energy requirements of 1.0 and 1.5 GeV. We also present the $\langle M_X^2 - \overline{M}_D^2 \rangle$ moment as a function of the lepton-energy cut. The M_X^2 moments with the 1.5 GeV lepton-energy requirement are in good agreement with CLEO's previously reported M_X^2 moments [21], obtained with the CLEO-II subset of the data used here. The results reported here, in addition to using more data, handle final-state radiation more carefully. These results supersede the previously published results.

The M_X^2 and q^2 moments reported here, moments of the lepton-energy spectrum previously reported [22], moments of the lepton energy spectrum over a broader energy range [23], and moments of the photon-energy spectrum in the radiative penguin decay $B \to X_s \gamma$ [20] can all be interpreted in the context of the HQET-OPE framework. The measurements should collectively provide a good determination of the HQET-OPE nonperturbative parameters $\overline{\Lambda}$ and λ_1, provide constraints on the $\mathcal{O}(\Lambda_{\mathrm{QCD}}^3/M_B^3)$ nonperturbative parameters ρ_1, ρ_2, $\mathcal{T}_1$, $\mathcal{T}_2$, $\mathcal{T}_3$, and $\mathcal{T}_4$, and provide a test of the quark-hadron duality assumption. An interpretation of this body of CLEO data, taking proper account of the correlations among the errors, is in preparation [24]. Here we give

TABLE VI. Correlation coefficients of the moments measurements presented in Table V.

Moment	Cut (GeV)	Correlation Coefficients							
$\langle M_X^2 - \overline{M}_D^2 \rangle$	$E_\ell > 1.0$ GeV	1.000	0.910	0.970	0.881	−0.795	−0.651	−0.034	−0.122
$\langle M_X^2 - \overline{M}_D^2 \rangle$	$E_\ell > 1.5$ GeV		1.000	0.824	0.856	−0.814	−0.784	−0.103	−0.179
$\langle (M_X^2 - \langle M_X^2 \rangle)^2 \rangle$	$E_\ell > 1.0$ GeV			1.000	0.884	−0.683	−0.523	0.054	−0.036
$\langle (M_X^2 - \langle M_X^2 \rangle)^2 \rangle$	$E_\ell > 1.5$ GeV				1.000	−0.606	−0.531	0.116	0.052
$\langle q^2 \rangle$	$E_\ell > 1.0$ GeV					1.000	0.925	0.301	0.352
$\langle q^2 \rangle$	$E_\ell > 1.5$ GeV						1.000	0.406	0.442
$\sqrt{\langle (q^2 - \langle q^2 \rangle)^2 \rangle}$	$E_\ell > 1.0$ GeV							1.000	0.979
$\sqrt{\langle (q^2 - \langle q^2 \rangle)^2 \rangle}$	$E_\ell > 1.5$ GeV								1.000

TABLE VII. $\langle M_X^2 - \overline{M}_D^2 \rangle$ versus the lepton-energy cut. The errors on the entries in the table are the statistical, detector systematic, and model-dependence uncertainties, respectively.

Cut (GeV)	$\langle M_X^2 - \overline{M}_D^2 \rangle$ (GeV$^2/c^4$)
$E_\ell > 1.0$	$0.456 \pm 0.014 \pm 0.045 \pm 0.109$
$E_\ell > 1.1$	$0.422 \pm 0.014 \pm 0.031 \pm 0.084$
$E_\ell > 1.2$	$0.393 \pm 0.013 \pm 0.027 \pm 0.069$
$E_\ell > 1.3$	$0.364 \pm 0.013 \pm 0.030 \pm 0.054$
$E_\ell > 1.4$	$0.332 \pm 0.012 \pm 0.027 \pm 0.055$
$E_\ell > 1.5$	$0.293 \pm 0.012 \pm 0.033 \pm 0.048$

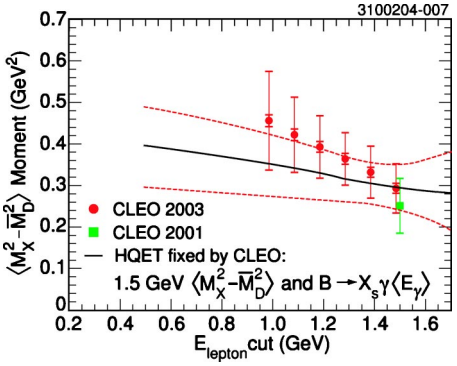

FIG. 3. $\langle M_X^2 - \overline{M}_D^2 \rangle$ versus lepton-energy cut. The "CLEO 2003" data points are from the work presented here and the "CLEO 2001" data point is from Ref. [21].

two examples of interpretation of the results presented in this paper.

In Fig. 3, we present a comparison of our results for the $\langle M_X^2 - \overline{M}_D^2 \rangle$ moment as a function of the lepton-energy cut with HQET-OPE predictions [25]. The $\overline{\Lambda}$ and λ_1 parameters are constrained by the first photon-energy moment of the $B \to X_s\gamma$ process [20] and the $\langle M_X^2 - \overline{M}_D^2 \rangle$ moment with a 1.5 GeV lepton-energy cut from this analysis. The theory bands shown in the figure reflect the experimental uncertainties on the two constraints, the variation of the third-order HQET

TABLE VIII. Contributions to systematic uncertainties of the moments measurements with a 1.0 GeV lepton-energy cut. The uncertainties due to the $B \to X_c \ell \nu$ nonresonant mass distribution and $B \to X_u \ell \nu$ models represent the range covered the set of models studied.

Variation	$\langle M_X^2 - \overline{M}_D^2 \rangle$ (GeV$^2/c^4$)	$\langle (M_X^2 - \langle M_X^2 \rangle)^2 \rangle$ (GeV$^4/c^8$)	$\langle q^2 \rangle$ (GeV$^2/c^4$)	$\sqrt{\langle (q^2 - \langle q^2 \rangle)^2 \rangle}$ ($10^{-3} \times$GeV$^2/c^4$)
Lepton Fake Rate	0.014/−0.006	0.047/−0.019	−0.011/0.006	−0.840/0.362
DELCO $b \to c \to \ell$ Shape	−0.008	−0.017	0.010	0.421
DELCO $+1\sigma$ $b \to c \to \ell$ Shape	−0.011	−0.021	0.015	0.574
DELCO -1σ $b \to c \to \ell$ Shape	−0.001	−0.005	−0.001	0.036
Continuum Norm ±10%	0.001/0.001	0.006/−0.029	0.015/−0.020	0.149/−0.198
μ Fakes, $E_\ell < 1.5$ GeV, ±10%	−0.011/0.011	−0.068/0.070	0.005/−0.003	0.803/−0.793
μ Fakes, $E_\ell > 1.5$ GeV, ±10%	−0.000/0.000	0.009/−0.009	0.001/−0.001	−0.044/0.049
$\mathcal{B}(b \to c \to \ell)$ ±10%	0.004/−0.003	−0.015/0.015	−0.006/0.006	−0.068/0.048
$\mathcal{B}(b \to$baryons) ±20%	0.002/−0.002	−0.011/0.011	0.003/−0.003	0.096/−0.104
No. K_L^0	0.003/−0.003	−0.018/0.019	−0.008/0.008	−0.061/0.033
Track Efficiency	0.002/−0.001	0.040/−0.041	0.003/−0.004	−0.288/0.257
No. Fake Tracks	−0.009/0.008	−0.041/0.038	0.005/−0.004	0.548/−0.506
Shower Efficiency	0.001/0.000	0.018/−0.016	0.006/−0.007	−0.069/−0.013
No. Fake Showers	−0.030/0.031	−0.181/0.172	0.013/−0.014	2.129/−2.164
Force Trk Multiplicity	0.002	0.003	−0.004	−0.120
Force Shwr Multiplicity	0.011	0.037	−0.003	−0.534
Final-State Radiation	0.021	0.088	−0.024	−1.567
Lepton Efficiency	0.006	0.022	−0.012	−0.499
Total Detector	0.045	0.222	0.094	3.130
$B \to D \ell \nu$ ρ Param.	−0.006/0.005	−0.016/0.004	0.022/−0.010	−7.112/5.057
$B \to D \ell \nu$ c_D Param.	−0.001/0.001	−0.000/−0.000	0.000/0.001	5.850/−4.784
$B \to D^* \ell \nu$ ρ Param.	−0.020/0.025	−0.045/0.046	0.041/−0.059	26.712/−27.140
$B \to D^* \ell \nu$ c_{A_1} Param.	0.003/−0.002	0.015/−0.010	−0.010/0.006	26.477/−26.716
$B \to D^* \ell \nu$ R1/R2 1st Eig. Vec.	0.019/−0.018	0.081/−0.070	−0.047/0.044	−19.883/19.427
$B \to D^* \ell \nu$ R1/R2 2nd Eig. Vec.	−0.000/0.000	0.028/−0.028	−0.006/0.005	−1.072/0.859
$B \to D^{**} \nu$ HQET Model	0.008	0.007	−0.014	10.384
$B \to D^{**} \ell \nu$ w Slope	0.014/−0.014	0.077/−0.058	−0.013/0.015	12.122/−11.871
$B \to X_c \ell \nu$ Nonres w Slope	0.008/−0.005	0.050/−0.031	−0.006/0.003	2.837/−1.456
$B \to X_c \ell \nu$ Nonres Mass	0.102/−0.078	0.615/−0.543	−0.058/0.029	5.928/−4.284
$B \to X_u \ell \nu$ Model	0.009/−0.012	0.018/−0.039	−0.004/0.005	−0.339/0.580
Total Model	0.109	0.631	0.100	47.10

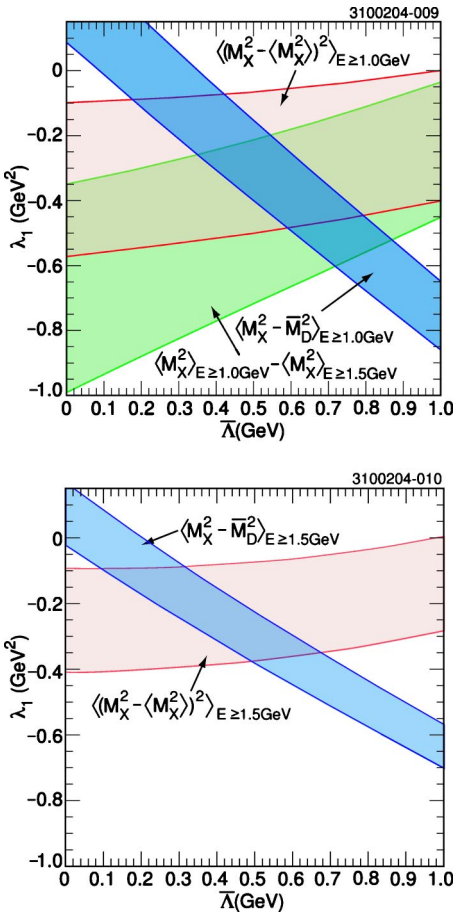

FIG. 4. Constraints on the nonperturbative parameters $\overline{\Lambda}$ and λ_1 due to the $\langle M_X^2 - \overline{M}_D^2 \rangle$ and $\langle (M_X^2 - \langle M_X^2 \rangle)^2 \rangle$ moment measurements with minimum lepton-energy requirement of 1.0 GeV and the $\langle M_X^2 \rangle_{E_\ell \geq 1.0\,\mathrm{GeV}} - \langle M_X^2 \rangle_{E_\ell \geq 1.5\,\mathrm{GeV}}$ moment measurement (left). Constraints on the nonperturbative parameters $\overline{\Lambda}$ and λ_1 due to the $\langle M_X^2 - \overline{M}_D^2 \rangle$ and $\langle (M_X^2 - \langle M_X^2 \rangle)^2 \rangle$ moment measurements with minimum lepton-energy requirement of 1.5 GeV (right).

parameters by the scale $(0.5\ \mathrm{GeV})^3$, and variation of the size of the higher order QCD corrections [25]. The theoretical calculation and the results of this measurement appear to agree. The more detailed analysis, in preparation [24], using the correlations of the measurements will provide a more stringent test of the prediction of the HQET-OPE theory. A violation of quark-hadron duality could manifest itself as a discrepancy in this calculation.

In Fig. 4, we show the bands in $\overline{\Lambda} - \lambda_1$ space defined by the $\langle M_X^2 - \overline{M}_D^2 \rangle$, the $\langle (M_X^2 - \langle M_X^2 \rangle)^2 \rangle$, and the $\langle M_X^2 \rangle_{E_\ell \geq 1.0\,\mathrm{GeV}} - \langle M_X^2 \rangle_{E_\ell \geq 1.5\,\mathrm{GeV}}$ moment measurements. The widths of the bands reflect the experimental uncertainties on the measured quantity, the variation of the third-order HQET parameters by the scale $(0.5\ \mathrm{GeV})^3$, and variation of the size of the higher order QCD corrections [25]. As shown Table VI, there are strong correlations among the errors, and hence a simple band plot only gives a qualitative indication of the values of $\overline{\Lambda}$ and λ_1. A precise determination, with errors, awaits the full analysis in preparation [24]. The extracted values of these parameters, when combined with precision measurements of the $B \to X_c \ell \nu$ branching fraction [23] and the B meson lifetime [8], permit the extraction of $|V_{cb}|$ with reduced theoretical uncertainties.

Note added. During the final preparation of this paper, we learned of a report from the BaBar Collaboration reporting new measurements of the first four hadronic mass moments [26]. The second and fourth hadronic mass moments reported by BaBar correspond to the first and second hadronic mass-squared moments reported here and are consistent within the quoted uncertainties. The BaBar measurements are based on an approximately nine times larger $\Upsilon(4S)$ sample and use a significantly different analysis technique. Their technique results in a larger statistical uncertainty and a smaller systematic uncertainty. The combined statistical and systematic uncertainties of the BaBar measurements range from half the uncertainty quoted here to similar uncertainty for the various comparable measurements.

ACKNOWLEDGMENTS

We gratefully acknowledge the effort of the CESR staff in providing us with excellent luminosity and running conditions. M. Selen thanks the Research Corporation, and A. H. Mahmood thanks the Texas Advanced Research Program. This work was supported by the National Science Foundation, and the U.S. Department of Energy.

[1] J. Chay, H. Georgi, and B. Grinstein, Phys. Lett. B **247**, 399 (1990); I. I. Bigi, M. A. Shifman, N. G. Uraltsev, and A. I. Vainshtein, Phys. Rev. Lett. **71**, 496 (1993); A. V. Manohar and M. B. Wise, Phys. Rev. D **49**, 1310 (1994).

[2] Y. Kubota *et al.*, Nucl. Instrum. Methods Phys. Res. A **320**, 66 (1992).

[3] T. S. Hill, Nucl. Instrum. Methods Phys. Res. A **418**, 32 (1998).

[4] G. C. Fox and S. Wolfram, Phys. Rev. Lett. **41**, 1581 (1978).

[5] A. V. Manohar and M. B. Wise, Cambridge Monogr. Part. Phys. Nucl. Phys. Cosmol. **10**, 1 (2000), provides a review and references to the orignal papers.

[6] R. J. Barlow and C. Beeston, Comput. Phys. Commun. **77**, 219 (1993).

[7] R. Brun *et al.*, CERN Report No. DD/EE/84-1, 1987.

[8] Particle Data Group, K. Hagiwara *et al.*, Phys. Rev. D **66**, 010001 (2002).

[9] D. Scora and N. Isgur, Phys. Rev. D **52**, 2783 (1995).

[10] J. L. Goity and W. Roberts, Phys. Rev. D **51**, 3459 (1995).

[11] Particle Data Group Collaboration, C. Caso *et al.*, Eur. Phys. J. C **3**, 1 (1998).

[12] T. Sjostrand, Comput. Phys. Commun. **39**, 347 (1986); T. Sjostrand and M. Bengtsson, *ibid.* **43**, 367 (1987).

[13] E. Barberio and Z. Wąs, Comput. Phys. Commun. **79**, 291 (1994).

[14] CLEO Collaboration, N. E. Adam *et al.*, Phys. Rev. D **67**, 032001 (2003).
[15] D. Atwood and W. J. Marciano, Phys. Rev. D **41**, 1736 (1990).
[16] E. Richter-Wąs, Phys. Lett. B **303**, 163 (1993).
[17] C. G. Boyd, B. Grinstein, and R. F. Lebed, Phys. Lett. B **353**, 306 (1995); I. Caprini and M. Neubert, *ibid.* **380**, 376 (1996); C. G. Boyd, B. Grinstein, and R. F. Lebed, Phys. Rev. D **56**, 6895 (1997); I. Caprini, L. Lellouch, and M. Neubert, Nucl. Phys. **B530**, 153 (1998).
[18] A. K. Leibovich, Z. Ligeti, I. W. Stewart, and M. B. Wise, Phys. Rev. D **57**, 308 (1998).
[19] F. De Fazio and M. Neubert, J. High Energy Phys. **06**, 017 (1999).
[20] CLEO Collaboration, S. Chen *et al.*, Phys. Rev. Lett. **87**, 251807 (2001).
[21] CLEO Collaboration, D. Cronin-Hennessy *et al.*, Phys. Rev. Lett. **87**, 251808 (2001).
[22] CLEO Collaboration, R. A. Briere *et al.*, hep-ex/0209024.
[23] CLEO Collaboration, A. H. Mahmood *et al.*, following paper, Phys. Rev. D **70**, 032003 (2004).
[24] CLEO Collaboration (in preparation).
[25] C. W. Bauer, Z. Ligeti, M. Luke, and A. V. Manohar, Phys. Rev. D **67**, 054012 (2003).
[26] BABAR Collaboration, B. Aubert, hep-ex/0403031.